
Figures and figure supplements

Nucleo-cytoplasmic shuttling of splicing factor SRSF1 is required for development and cilia function

Fiona Haward *et al*

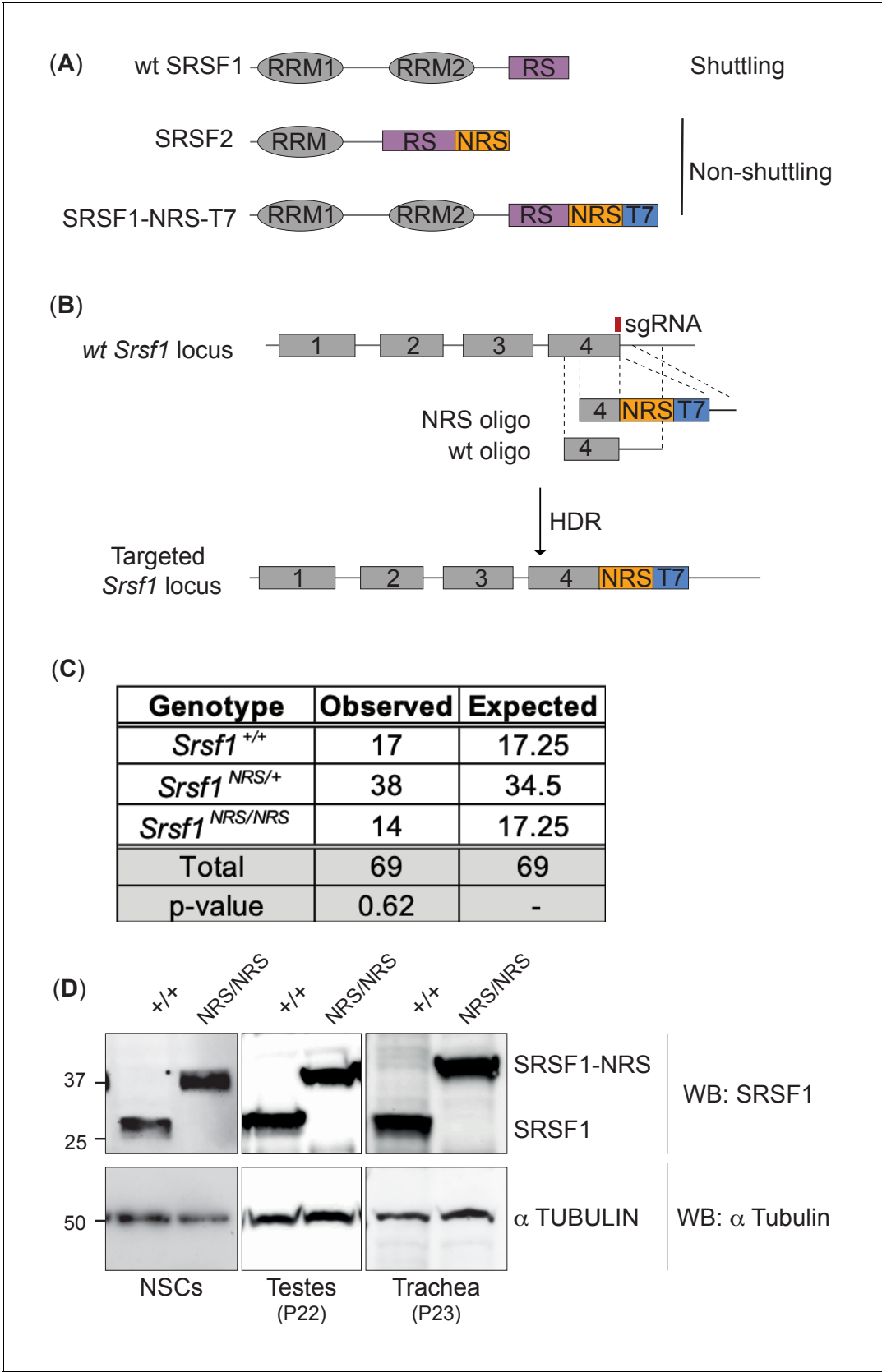


Figure 1. Generation of a nuclear-restrained SRSF1 (*Srsf1*^{NRS/NRS}) knock-in mouse model. (A) Domain structure and nucleo-cytoplasmic shuttling ability of wild-type (WT) SRSF1 and SRSF2 proteins, and the artificial fusion protein SRSF1-NRS. (B) Schematic representation of the *Srsf1* locus and the

Figure 1 continued on next page

Figure 1 continued

CRISPR/Cas9 strategy used to introduce an NRS-T7 sequence at its C-terminus. The nucleotide sequence of the introduced nuclear retention signal (NRS) is identical to that present in the endogenous mouse *Srsf2* gene (Cazalla et al., 2002). (C) *Srsf1*^{NRS/NRS} homozygous knock-in mice complete embryogenesis and are viable postnatally. The number of pups obtained from *Srsf1*^{+/NRS} intercrosses with indicated genotypes at postnatal day 14 are indicated. The expected Mendelian numbers and χ^2 -test p value (p=0.62, n = 69) are also shown. (D) Expression of SRSF1 and SRSF1-NRS proteins in neuronal stem cells (NSCs), testes, and trachea derived from *Srsf1*^{NRS/NRS} mice at the indicated postnatal age. An anti-SRSF1 antibody was used for western blot analysis to detect both the endogenous SRSF1 protein, as well as the knock-in protein (SRSF1-NRS), whereas anti-tubulin was used as a loading control.

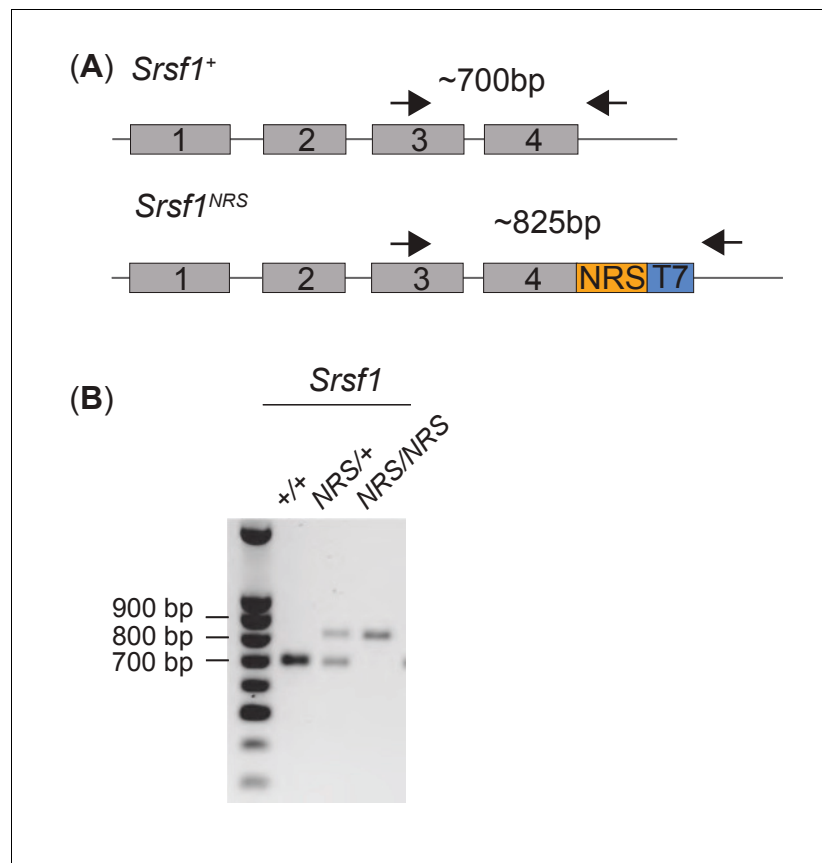


Figure 1—figure supplement 1. Genotyping of *Srsf1*^{NRS/NRS} mice. (A) Schematic of the PCR-based genotyping strategy adopted to determine the knock-in status of the C-terminal region of endogenous SRSF1. The arrows represent primers used for PCR. Amplicon sizes for the *Srsf1*^{NRS} or *Srsf1*^{wt} are shown. (B) PCR analysis of genomic DNA of the first two cohorts of pups from heterozygous intercrosses. The PCR products of animals selected for use were all subject to Sanger sequencing to confirm the presence of an intact *Srsf1*^{NRS} allele at the correct genomic locus. Representative samples are shown.

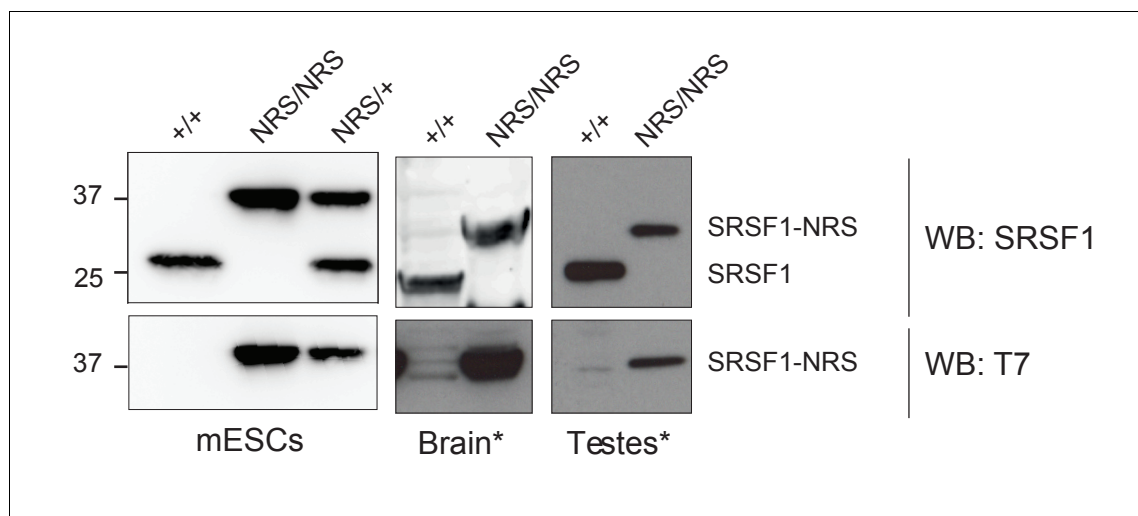


Figure 1—figure supplement 2. Expression of SRSF1 and SRSF1-NRS protein in cell lines and tissues derived from *Srsf1*^{+/+} and *Srsf1*^{NRS/NRS} mice. Either SRSF1 or T7 antibodies were used for western blot analysis to detect both the endogenous untagged protein (SRSF1) and the knock-in protein (SRSF1-NRS). * indicates that blots presented for SRSF1 and T7 are not from the same membrane but instead two different westerns of those tissues.

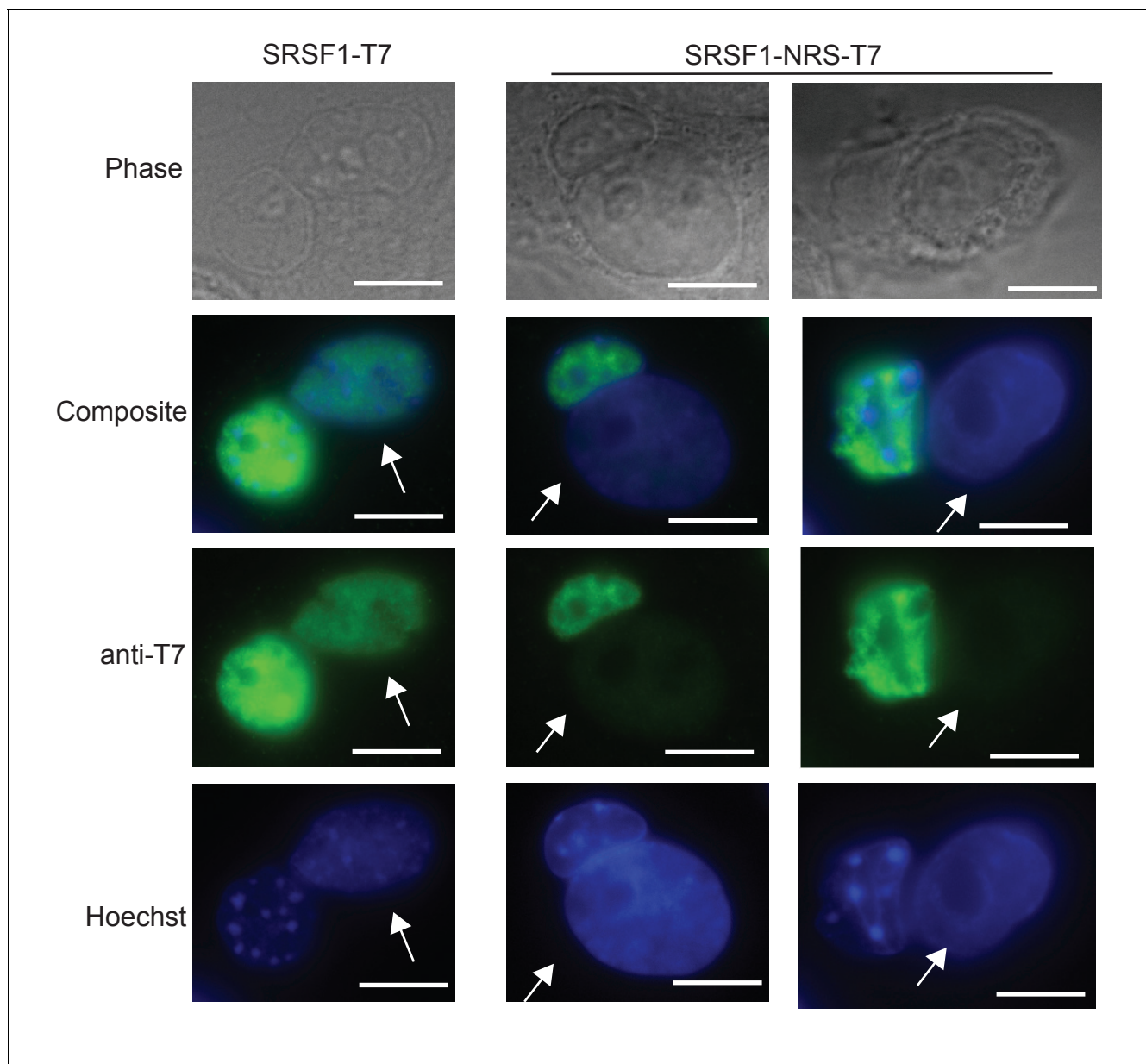


Figure 1—figure supplement 3. Localization of SRSF1 and SRSF1-NRS protein. Analysis of nucleo-cytoplasmic shuttling of SRSF1-NRS in neuronal stem cells (NSCs) using a heterokaryon assay. Briefly, mouse NSCs (donor) from controls (wild-type NSCs transfected with wild-type T7-tagged SRSF1; left column) or *Srsf1*^{NRS/NRS} NSCs (right columns) were differentiated from ES cells derived from mice. Human HeLa cells (recipient) were subsequently fused with mouse NSCs (donor) in the presence of cycloheximide to form heterokaryons. The cells were incubated further for 3 hr in the presence of cycloheximide and fixed. The localization of SRSF1 was determined with anti-T7 monoclonal antibody. Hoechst 33258 was used to differentially stain mouse and human nuclei. Human (recipient) nuclei are depicted (white arrow). Scale bar, 10 μ m.

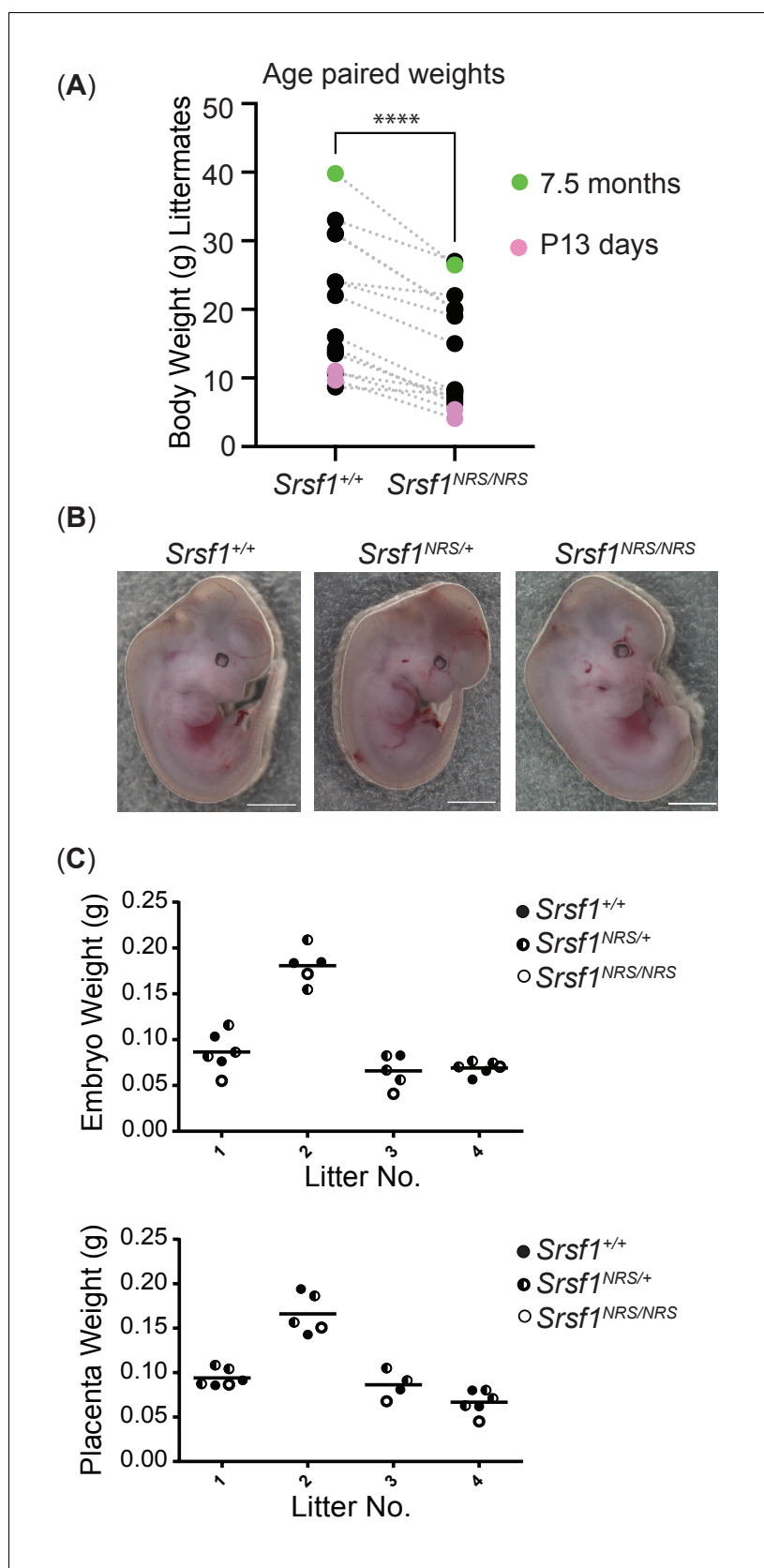


Figure 2. Homozygosity for the *Srsf1*^{NRS} allele causes postnatal growth restriction. (A) Whole-body weight of sex-matched littermate pairs indicated by connecting lines. Animals range from 13 days (pink) to 7.5 months old (blue). Figure 2 continued on next page

Figure 2 continued

N = 15 animals/genotype. (B) *Srsf1*^{NRS/NRS} knock-in embryos at E13.5 are grossly phenotypically normal. *Srsf1*^{NRS/NRS} embryos were represented in these litters at the expected Mendelian ratio (7 *Srsf1*^{+/+}, 11 *Srsf1*^{+/NRS}, 4 *Srsf1*^{NRS/NRS}; χ^2 p value = 0.66). (C) Scatter plots showing the weight of whole embryos (top panel) and of placentas from four independent litters of E12.5 embryos (bottom panel).

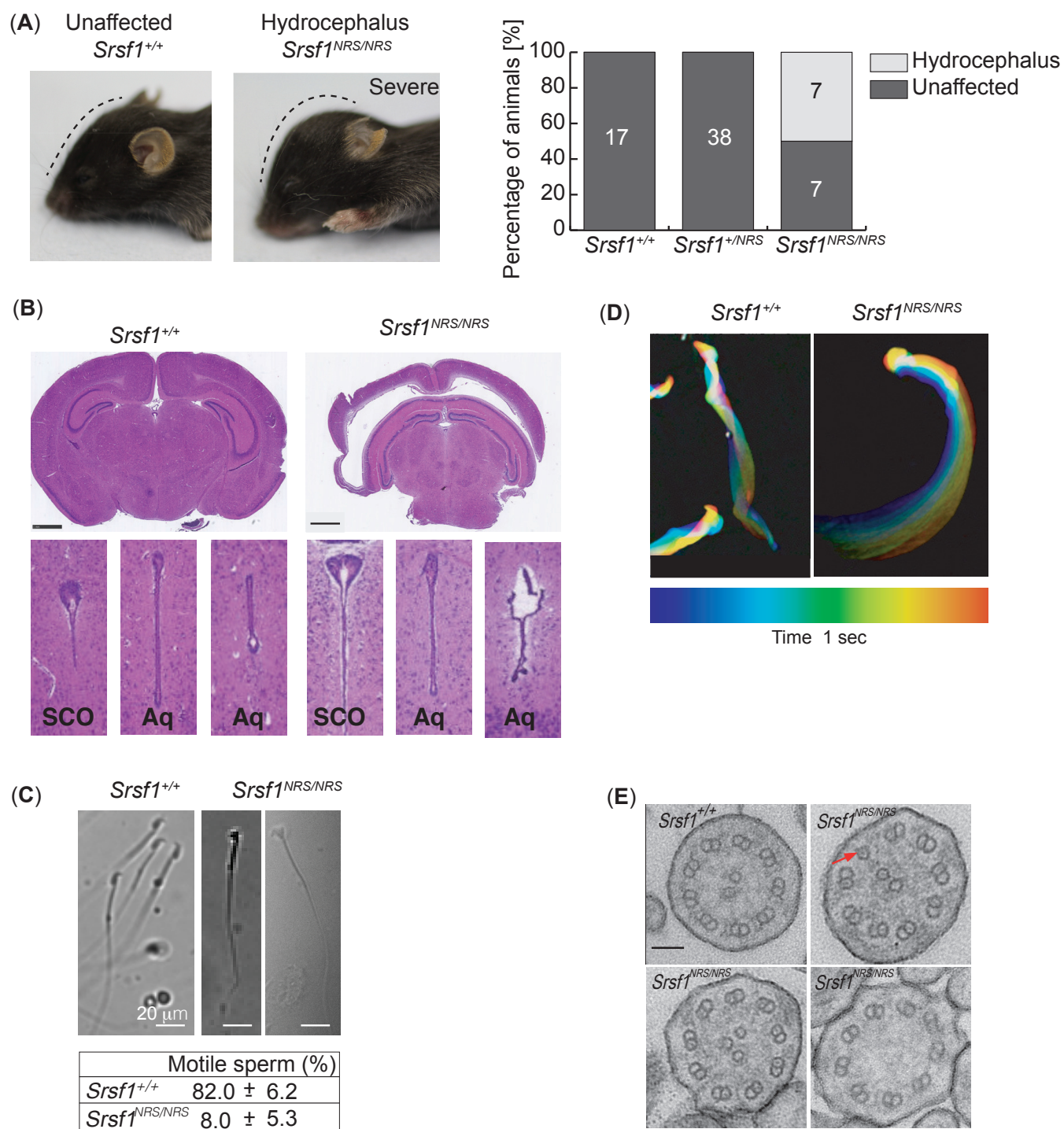


Figure 3. Homozygous *Srsf1*^{NRS/NRS} mice develop hydrocephalus. **(A)** *Srsf1*^{NRS/NRS} mice show signs of developing hydrocephalus (the curvature of the skull is depicted by a dashed line). Half of the mice culled from the first two cohorts developed externally visible hydrocephalus of a varying severity by P14, while hydrocephalus was not observed in *Srsf1*^{+/+} or *Srsf1*^{NRS/+} littermates. The bar plot indicates the incidence of mice unaffected or with gross hydrocephalus (percentage and total number) in the two cohorts of mice used (p-value=0.0013 and <0.0001, respectively; Fischer's exact test). **(B)** H&E staining of coronal sections of brains at subcommissural organ (SCO) and aqueducts (Aq) of third and fourth ventricles show no overt stenosis. Scale bar: 1 mm. **(C)** Representative images illustrate abnormal head shape of some spermatozoa observed in *Srsf1*^{NRS/NRS} littermates. Bottom panel shows Figure 3 continued on next page

Figure 3 continued

percentage of motile sperm ($N \geq 3$ animals per genotype). (D) Color coding illustrates that the complex rotational pattern of *Srsf1*^{+/+} spermatozoa, required to propel the sperm forward, is absent in the few motile *Srsf1*^{NRS/NRS} spermatozoa. (E) Transmission electron microscopy of transverse sections of mouse tracheal epithelial culture (mTEC) cilia showing (9+2) microtubules in *Srsf1*^{+/+} or abnormal variations found in *Srsf1*^{NRS/NRS}. Red arrow illustrates microtubule singlet. Scale bar: 100 nm.

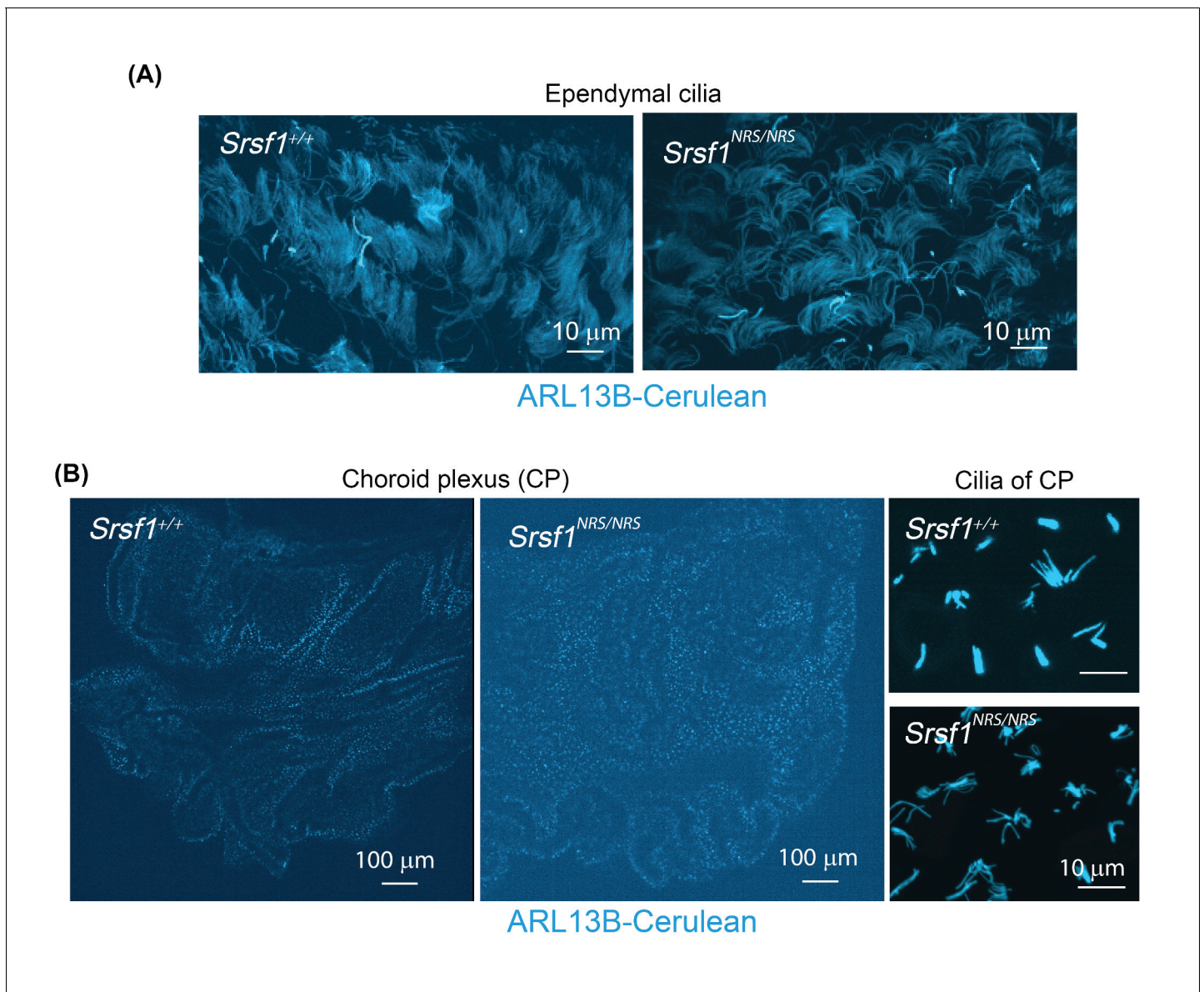


Figure 3—figure supplement 1. Live images of ependymal cells and choroid plexus from *R26Arl13b-Fucci2aR^{Tg/Tg},Srsf1^{+/+}* and *R26Arl13b-Fucci2aR^{Tg/Tg},Srsf1^{NRS/NRS}* (P27) mice. (A) Ependymal cells from lateral ventricles (B) Choroid plexus of lateral ventricles. Both cases show a comparable number and distribution of ciliary bundles between *Srsf1^{NRS/NRS}* and *Srsf1^{+/+}* littermates.

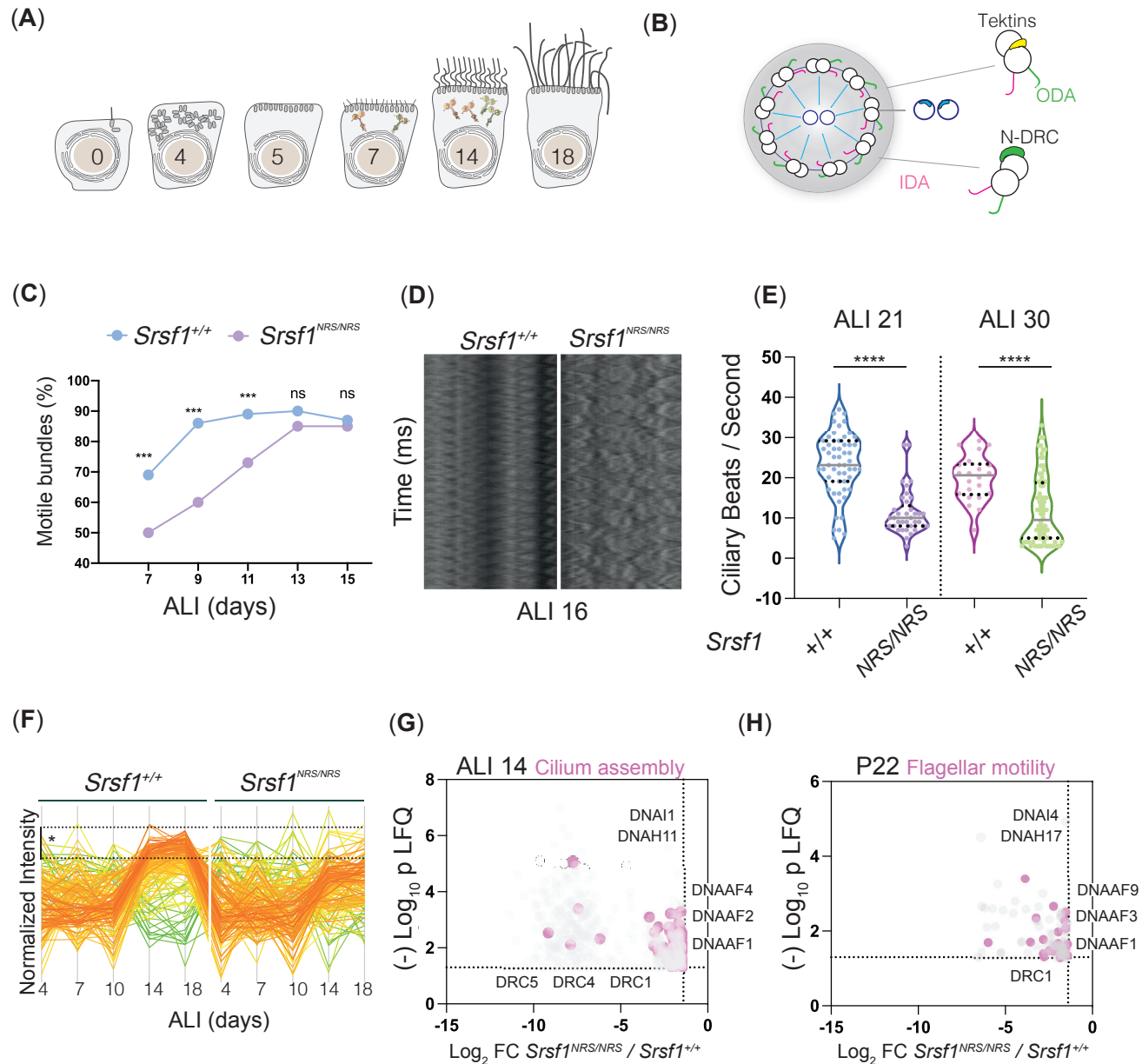


Figure 4. Molecular studies of *Srsf1*^{NRS/NRS} mice are consistent with defects in ciliary motility. (A) Diagram depicts landmark events in the maturation of motile cilia in mouse tracheal epithelial cultures (mTECs), upon culture in air-liquid interface (ALI) as days post airlift. Stages depicted include centriole amplification and apical docking (ALI 4–6), burst of synthesis, and assembly of motile ciliary machinery concomitant with growth and ciliary elongation (ALI 7–14) continuous ciliary beat maturation (ALI 18). (B) Diagram of a motile axoneme and some auxiliary components. N-DRC: nexin-dynein regulatory complexes; ODA: outer dynein arm; IDA: inner dynein arm. (C) Percentage of motile ciliary bundles during mTEC differentiation. N = 2 animals/genotype at ALI7 and ALI9; N = 3 at all later stages. More than >100 ciliary bundles were scored at each time point exact test at each stage. (D) Representative kymographs of motile bundles illustrate differences in beating amplitude at stages late stages, ALI 16. (E) Cilia beat frequency of *Srsf1*^{NRS/NRS} and *Srsf1*^{+/+} tracheal cultures grown in parallel at the indicated differentiation stages. Asterisks denote $p < 0.001$ determined by Mann–Whitney tests as *Srsf1*^{NRS/NRS} ciliary movement does not follow a normal distribution. (F) Z-normalized intensities of proteins containing ‘cilia’ within their GO term aligned along tracheal stages (ALI4–18) and genotypes. Each line represents a single protein, where color coding denotes those that match closely to the mean trajectory of the group (red) from those that deviate (green). This shows that *Srsf1*^{+/+} induces the coordinated expression of multiple cilia-associated proteins during maturation with a greater amplitude than *Srsf1*^{NRS/NRS}. Note the tighter distribution of trajectories, and greater fold change (FC) in *Srsf1*^{+/+} samples (*). (G, H) Volcano plots of proteins that are significantly under-represented in *Srsf1*^{NRS/NRS} cultures at ALI14 (G) and P22 (H).

Figure 4 continued

testes at P22 (H). Pink dots represent proteins with cilia in their GO term. Label-free quantitation (LFQ) values, analysis, and protein identity of data presented in panels (G) and (H) can be found in **Figure 4—source data 1**.

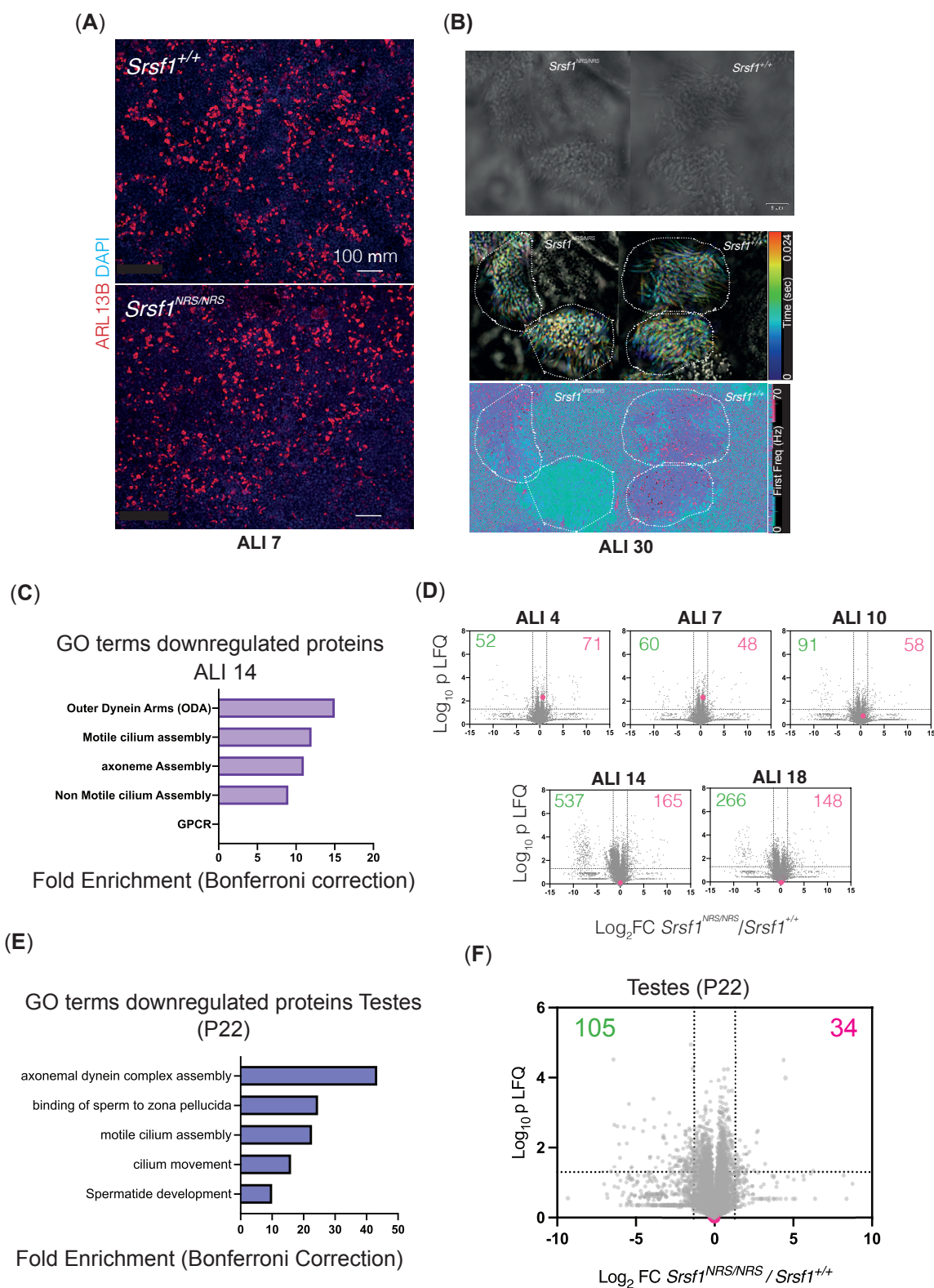


Figure 4—figure supplement 1. Nuclear sequestration of SRSF1 leads to alterations in total proteomes consistent with defects in cilia motility observed during mouse tracheal epithelial culture (mTEC) differentiation. (A) Immunofluorescence of mTECs at ALI7 showing comparable number of

Figure 4—figure supplement 1 continued on next page

Figure 4—figure supplement 1 continued

ciliated bundles (ARL13B stained) between *Srsf1*^{+/+} and *Srsf1*^{NRS/NRS} cultures. (B) High-speed imaging of mature mTECs (ALI30) shows different waveforms in *Srsf1*^{NRS/NRS} cilia. The still images show a single time frame of the bundles analyzed below. Middle: color-coded time projections applying the subtract background function in ImageJ. While neighbored cilia on *Srsf1*^{+/+} cells align their beat, cilia on *Srsf1*^{NRS/NRS} cells beat in a less coordinated. Bottom: frequency of the highest peak in the power spectrum derived by fast Fourier transformation of the intensity time course at each pixel, revealing the ciliary beat frequency of individual cells. (C) Functional GO terms enriched in downregulated proteins at ALI14 from *Srsf1*^{NRS/NRS} mTEC cultures (right panel). (D) Volcano plots at indicated time points illustrate proteins miss-regulated in *Srsf1*^{NRS/NRS} relative to *Srsf1*^{+/+} mTEC cultures. Number of proteins altered is shown in each quadrant. Red dots represent SRSF1 peptides. (E) Functional GO terms enriched in proteins found downregulated in *Srsf1*^{NRS/NRS} P22-23 testes. Excel tables containing LFQ values, analysis, and protein identity of data presented in panels (D) and (F) can be found in **Figure 4—figure supplement 1—source data 1**.

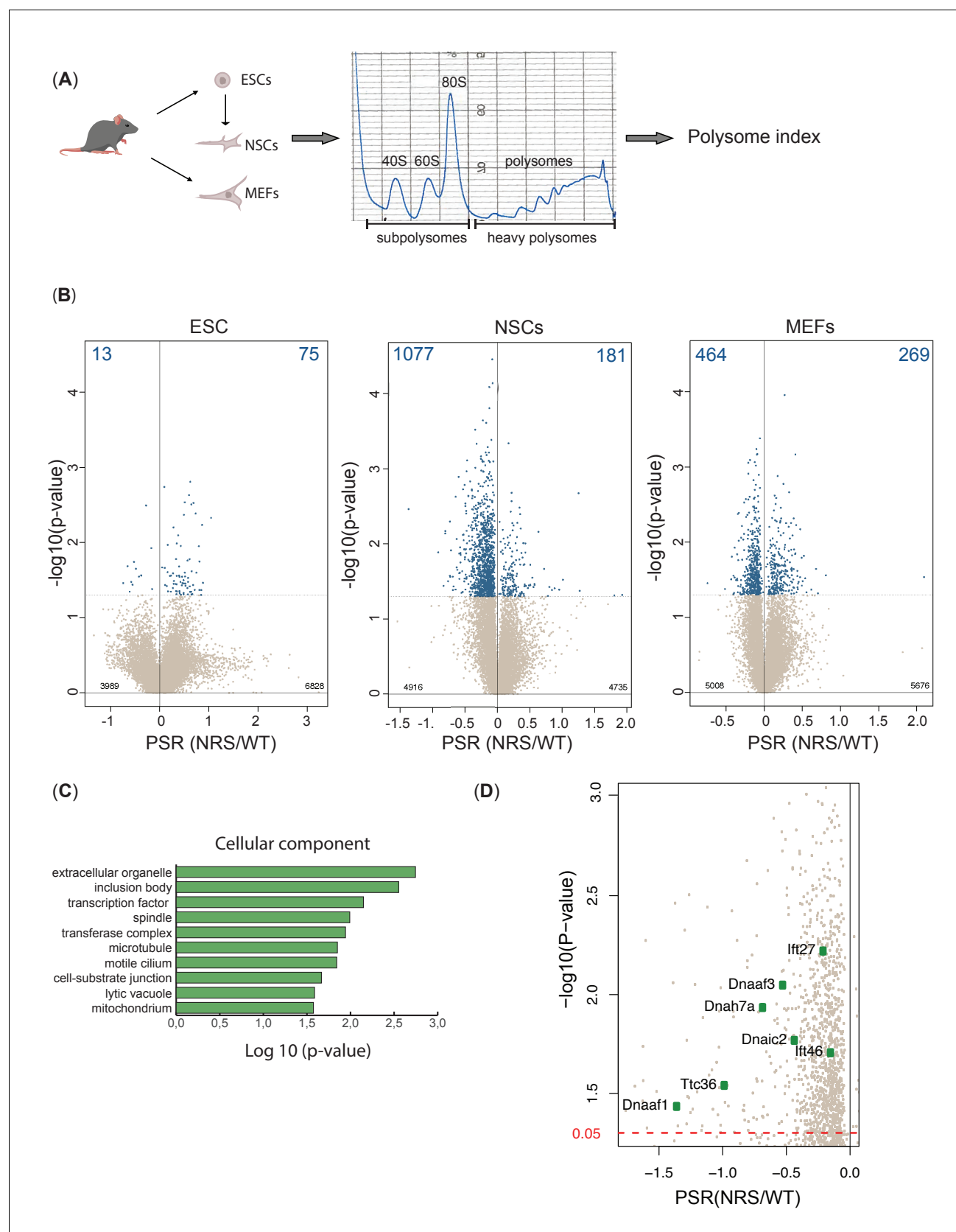


Figure 5. Lack of cytoplasmic SRSF1 results in gross changes in translation. (A) Schematic of the experimental approach used to identify translation profiles of wild-type SRSF1 or SRSF1-NRS-expressing ESCs, neuronal stem cells (NSCs), and mouse embryonic fibroblast (MEF) cells. A summary of a Figure 5 continued on next page

Figure 5 continued

fractionation profile is depicted. Absorbance at 254 nm was monitored. RNA isolated from the pooled subpolysomal and polysomal fractions was subjected to RNA sequencing. **(B)** Volcano plots showing the distribution of genes expressed in all cell lines according to their polysome shift ratio (PSR). PSR is calculated as a ratio of polysome index in *Srsf1*^{+/+} vs. *Srsf1*^{NRS/NRS} cells. Blue dots indicate significant changes. Number of significant changes is indicated in the top corners of each plot. **(C)** GO term overrepresentation analysis identifies spindle and motile cilium as enriched cellular components category in the downregulated PSR gene list. **(D)** Plot showing the distribution of genes expressed in NSCs with PSR < 0. Selected ciliary genes are highlighted.

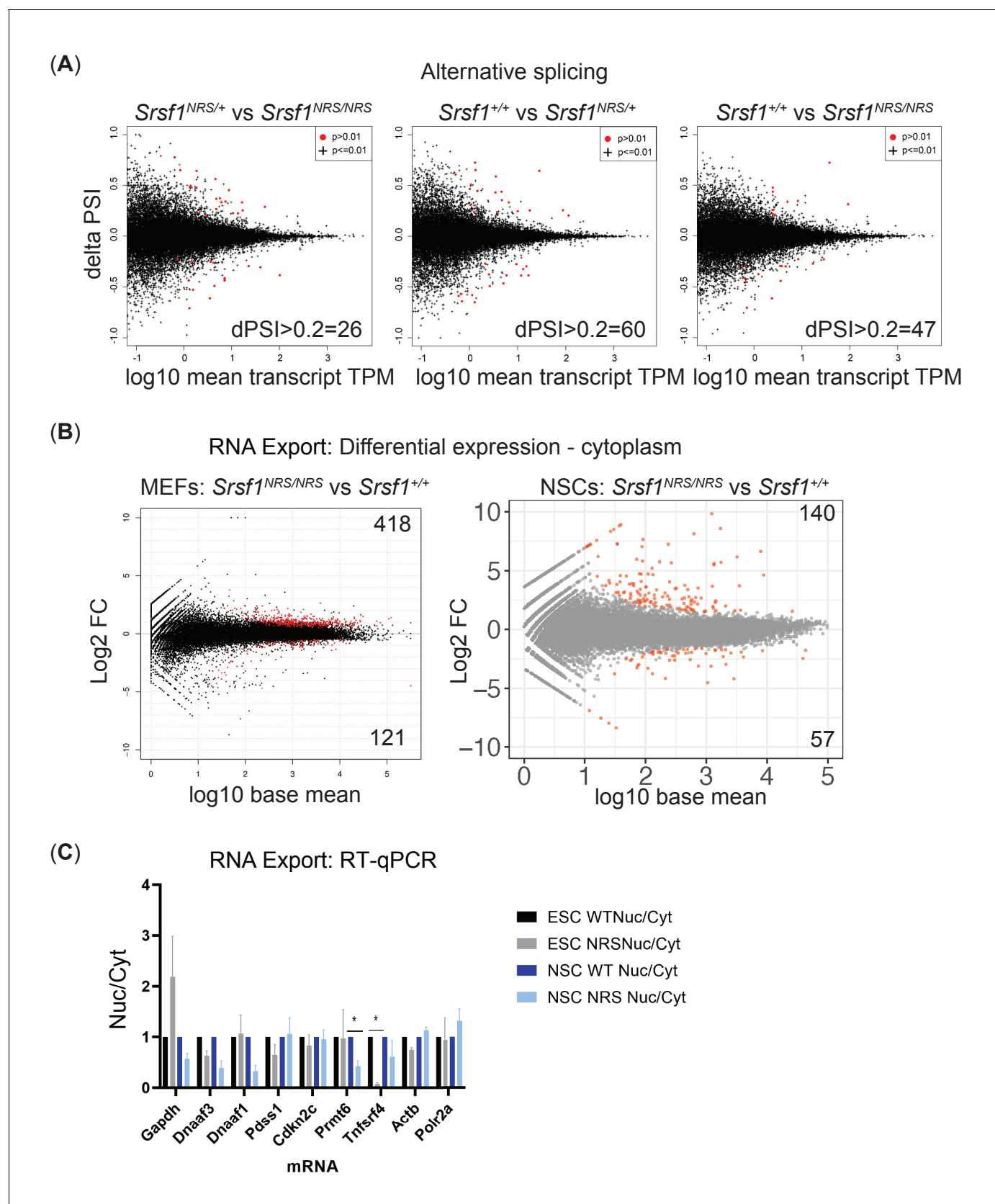


Figure 5—figure supplement 1. The lack of cytoplasmic SRSF1 does not affect pre-mRNA splicing or mRNA export. (A) Delta PSI scatter plots for knock-in mouse embryonic fibroblasts (MEFs). The number of changes (Δ PSI \Rightarrow 0.2, $p < 0.01$, TPM \Rightarrow 0.5) from indicated pairwise comparisons of Figure 5—figure supplement 1 continued on next page

Figure 5—figure supplement 1 continued

splicing changes between each genotype of SRSF1 knock-in mice is depicted. (B) Plot of the Log2 fold change of the cytoplasmic abundance of mRNAs between wild-type and SRSF1-NRS-expressing MEFs and neuronal stem cells (NSCs). (C) The nuclear-cytoplasmic ratio of individual mRNAs in wild-type or SRSF1-NRS expressing cells was quantified by RT-qPCR. The data is an average of three independent experiments, and each bar represents an average and a standard error. NRS: nuclear retention signal.

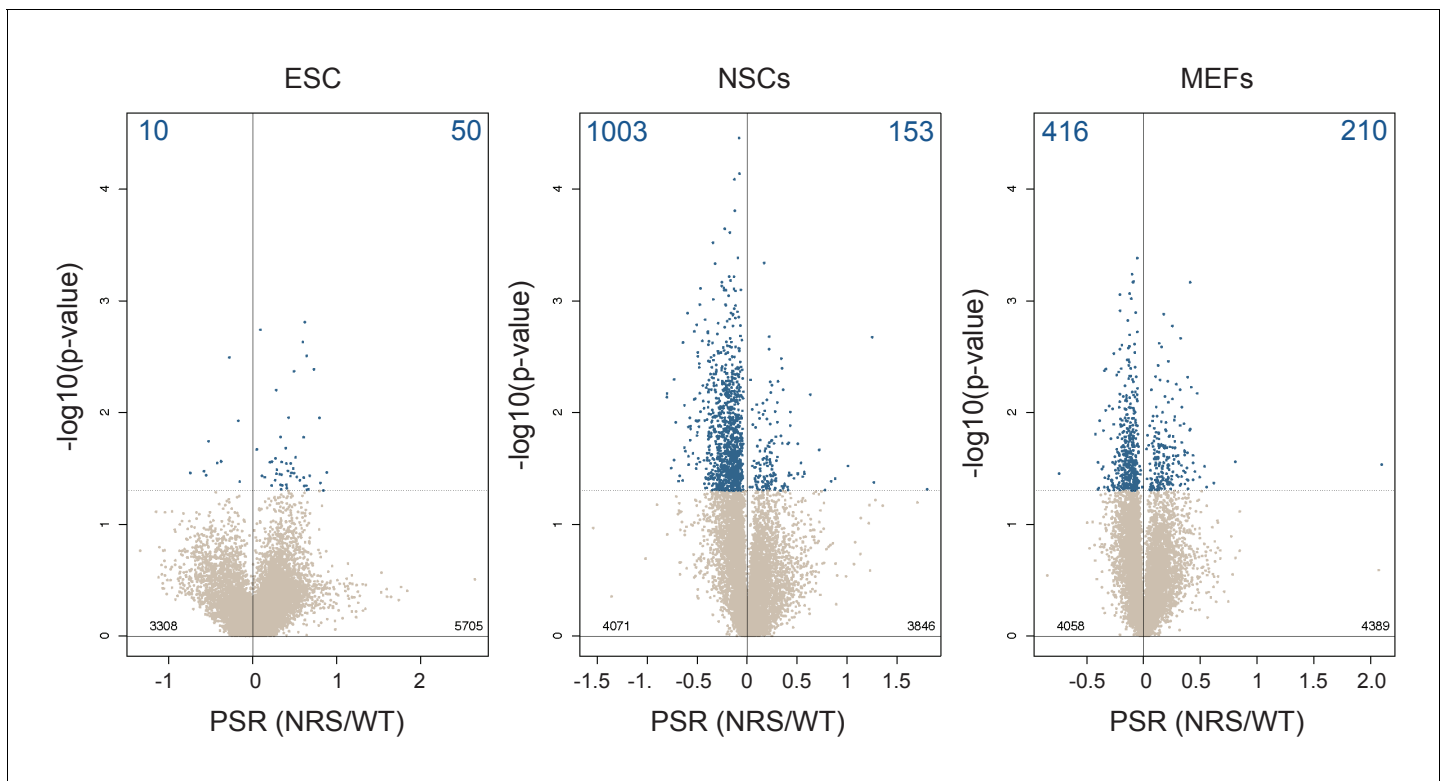


Figure 5—figure supplement 2. Lack of cytoplasmic SRSF1 induces translational changes not restricted to lineage-specific transcript. Scatter plots showing the distribution of genes expressed in each cell line according to their polysome shift ratio (PSR). Blue dots indicate significant changes (False discovery rate (FDR) < 0.05). Number of significant changes is indicated in the top corners of each plot.

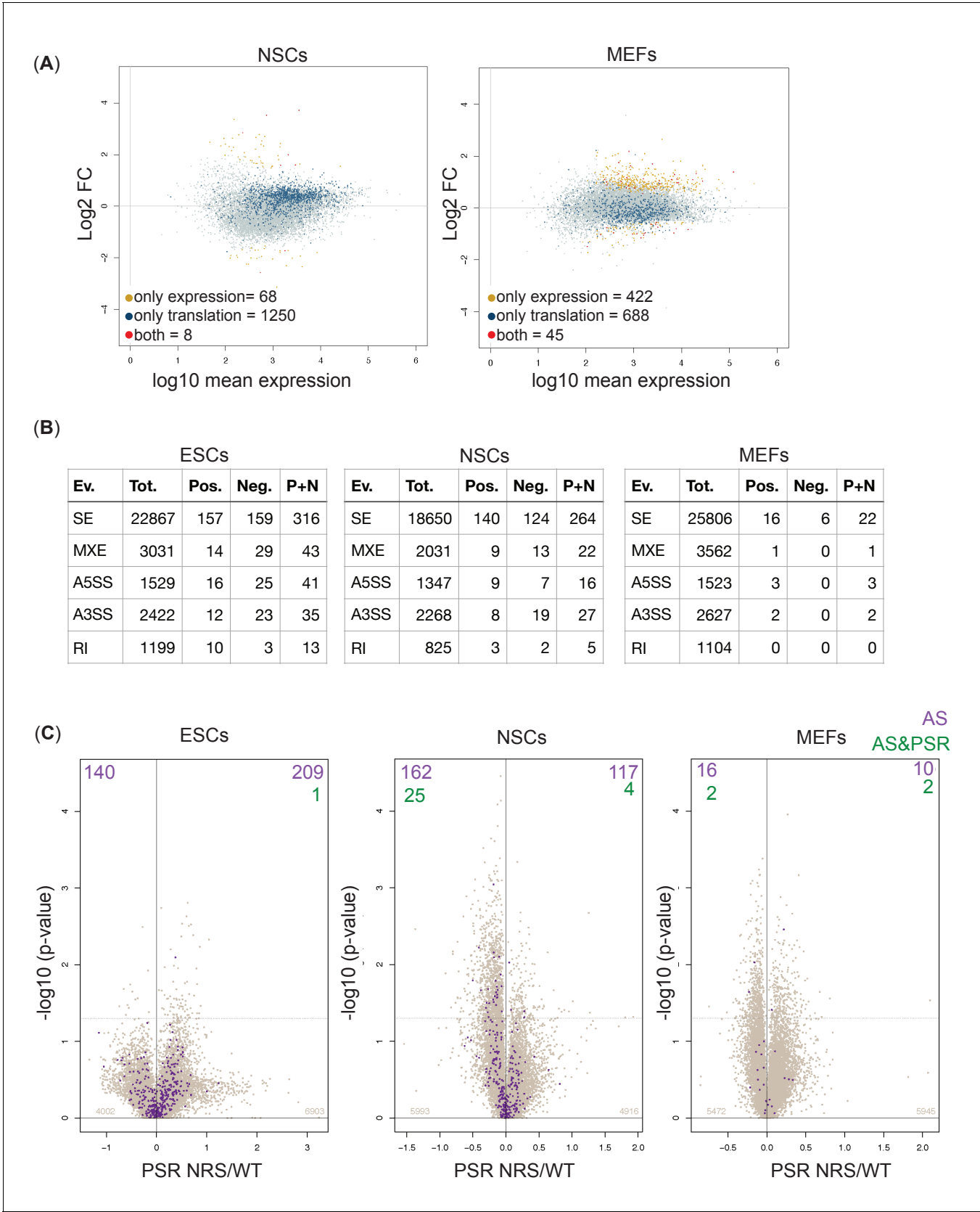


Figure 5—figure supplement 3. Polysome shift ratio (PSR) values are independent of alternative splicing and gene expression changes in cytoplasm. (A) Plot of the Log2 fold change of the cytoplasmic abundance of mRNAs between *Srsf1*^{+/+} and *Srsf1*^{NRS/NRS} cells. Yellow, dark blue, and red dots

Figure 5—figure supplement 3 continued on next page

Figure 5—figure supplement 3 continued

indicate significant changes in expression, in PSR or both expression and PSR, respectively. The number of genes affected at the level of expression, translation, or both is highlighted in the left corners of plots. **(B)** Number of alternative splicing changes detected between *Srsf1*^{+/+} and *Srsf1*^{NRS/NRS} cells. Ev: type of splicing event; SE: cassette exons; MXE: microexons; A5SS: alternative 5' splice site; A3SS: alternative 3' splice site; RI: intron retention. Tot. represents a total number of splicing events, Pos. and Neg. represent those splicing events that increase and decrease in *Srsf1*^{NRS/NRS} cells in comparison to *Srsf1*^{+/+} cells, respectively. **(C)** Scatter plots showing the distribution of genes expressed in all cell lines according to PSR. Purple dots indicate identified splicing changes. Number of significant splicing changes and significant splicing changes observed for genes with significant PSRs is indicated in the top corners of each plot (alternative splicing [AS] and AS and PSR, respectively).

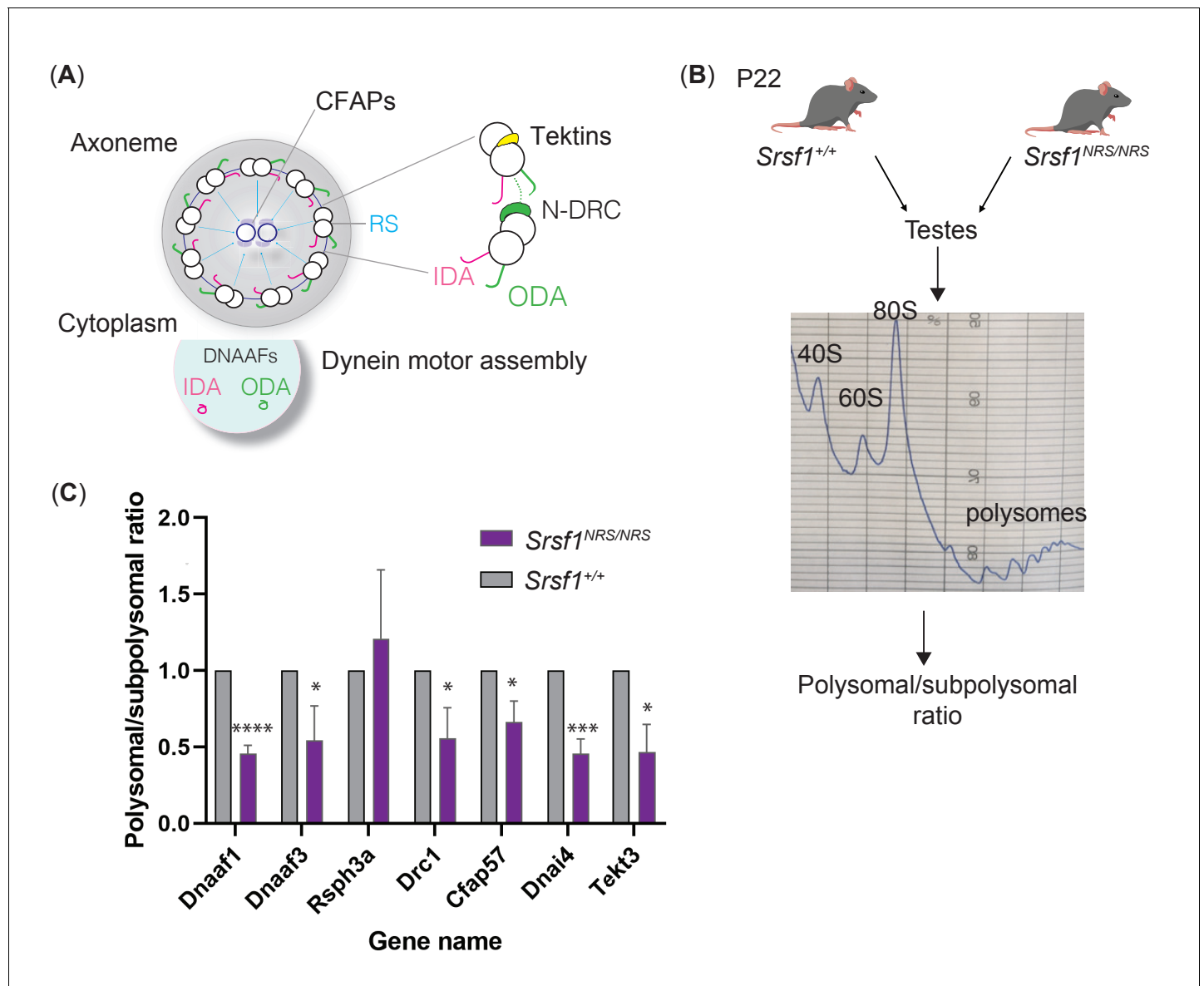


Figure 6. Lack of cytoplasmic SRSF1 results in gross changes in translation in mouse testes. (A) Summary schematic of functional groups under-represented in the total proteomes of tracheal cultures and maturing testes. (B) Schematic of the experimental approach used to identify translation profiles of *Srsf1*^{+/+} and *Srsf1*^{NRS/NRS} testes. A summary of a fractionation profile is depicted. Absorbance at 254 nm was monitored. RNA isolated from the pooled subpolysomal and polysomal fractions was subjected to RNA sequencing. (C) The polysomal-subpolysomal ratio of individual mRNAs in wild-type or SRSF1-NRS expressing testes was quantified by RT-qPCR. The data is an average of five independent experiments, and each bar represents an average and a standard error. Asterisks represent statistical significance; *p<0.05; ***p<0.0001; ****p<0.00001.

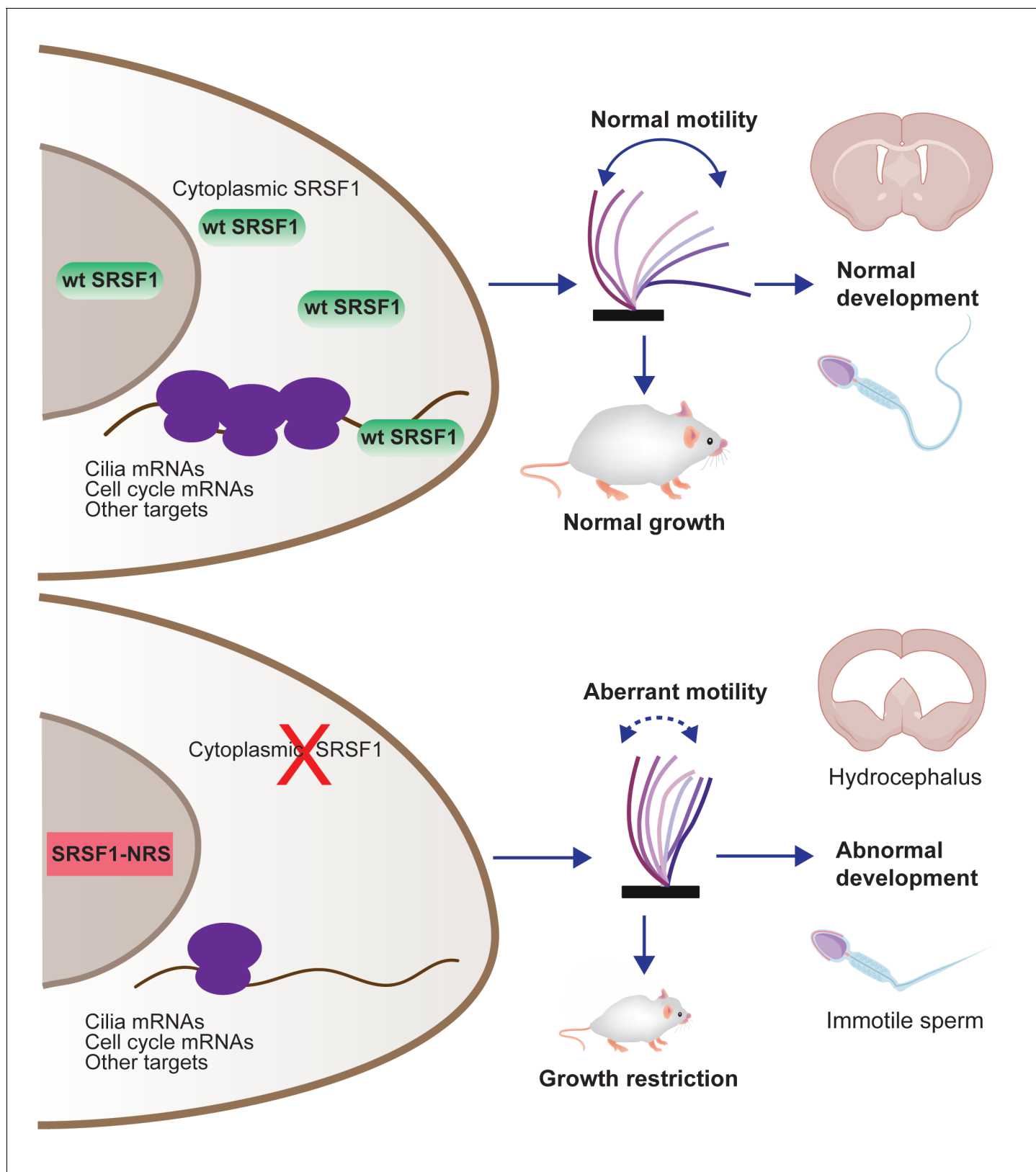


Figure 7. Restricting SRSF1 to the nucleus results in perinatal phenotypes in the mouse including growth, brain development, and spermatogenesis, particularly affecting motile cilia. This highlights the physiological role of splicing factor nucleocytoplasmic shuttling to reprogram gene expression networks to meet high cellular demands.